

CFD-Based Framework for Analysis of Soil–Pipeline Interaction in Reconsolidating Liquefied Sand

Pisano, F.; Cremonesi, Massimiliano; Cecinato, Francesco; Della Vecchia, Gabriele

DOI

[10.1061/\(ASCE\)EM.1943-7889.0001846](https://doi.org/10.1061/(ASCE)EM.1943-7889.0001846)

Publication date

2020

Document Version

Final published version

Published in

Journal of Engineering Mechanics

Citation (APA)

Pisano, F., Cremonesi, M., Cecinato, F., & Della Vecchia, G. (2020). CFD-Based Framework for Analysis of Soil–Pipeline Interaction in Reconsolidating Liquefied Sand. *Journal of Engineering Mechanics*, 146(10), Article 0001846. [https://doi.org/10.1061/\(ASCE\)EM.1943-7889.0001846](https://doi.org/10.1061/(ASCE)EM.1943-7889.0001846)

Important note

To cite this publication, please use the final published version (if applicable). Please check the document version above.

Copyright

Other than for strictly personal use, it is not permitted to download, forward or distribute the text or part of it, without the consent of the author(s) and/or copyright holder(s), unless the work is under an open content license such as Creative Commons.

Takedown policy

Please contact us and provide details if you believe this document breaches copyrights. We will remove access to the work immediately and investigate your claim.



CFD-Based Framework for Analysis of Soil–Pipeline Interaction in Reconsolidating Liquefied Sand

Federico Pisanò, Ph.D.¹; Massimiliano Cremonesi, Ph.D.²;
Francesco Cecinato, Ph.D.³; and Gabriele Della Vecchia, Ph.D.⁴

Abstract: Submarine buried pipelines interact with shallow soil layers that are often loose and prone to fluidization/liquefaction. Such occurrence is a possible consequence of pore pressure build-up induced by hydrodynamic loading, earthquakes, and/or structural vibrations. When liquefaction is triggered in sand, the soil tends to behave as a viscous solid–fluid mixture of negligible shear strength, possibly unable to constrain pipeline movements. Therefore, pipelines may experience excessive displacement, for instance, in the form of vertical flotation or sinking. To date, there are no well-established methods to predict pipe displacement in the event of liquefaction. To fill such a gap, this work proposes a computational fluid dynamics (CFD) framework enriched with soil mechanics principles. It is shown that the interaction between pipe and liquefied sand can be successfully analyzed via one-phase Bingham fluid modeling of the soil. Postliquefaction enhancement of rheological properties, viscosity, and yield stress can also be accounted for by linking soil–pipe CFD simulations to a separate analysis of the pore pressure dissipation. The proposed approach is thoroughly validated against the results of small-scale pipe flotation and pipe dragging tests from the literature. DOI: [10.1061/\(ASCE\)EM.1943-7889.0001846](https://doi.org/10.1061/(ASCE)EM.1943-7889.0001846). © 2020 American Society of Civil Engineers.

Introduction

Pipeline infrastructure is widely employed in offshore energy developments to transport hydrocarbons from wells to plants for processing and distribution. When directly laid on the seabed, pipelines are often exposed to harsh hydrodynamic loads that may negatively impact their structural performance. Although pipelines can usually withstand large displacements, the setup of suitable stabilization measures drives major costs in real projects (Cheuk et al. 2008; White and Cathie 2010). A typical stabilization option is to lay pipelines in trenches backfilled with rocks or sand. Pipe trenching can be very expensive but can increase the lateral resistance and drastically reduce hydrodynamic forces (Teh et al. 2006; Bai and Bai 2014).

Pipelines buried in sandy backfill may suffer from the consequences of soil liquefaction because backfills are inevitably loose (uncompacted) and shallow (i.e., at low effective stresses). Liquefaction can be triggered by a number of factors, including structural vibrations, ocean waves, tidal fluctuations, and earthquakes (Sumer et al. 1999; De Groot et al. 2006; Luan et al. 2008). Due to the low strength and stiffness of fluidized soils, segments of buried

pipelines may experience excessive displacements, for instance in the form of vertical flotation or sinking. In the presence of light pipelines, the large unit weight of liquefied sand is often the main flotation trigger. Reportedly, pipes may also float during/after trench backfilling due to the soil liquefaction phenomena taking place behind the backfill plough (Cathie et al. 1996).

Following the first pioneering studies in the United States (Pipeline Flotation Research Council 1966), North Sea offshore developments fostered in-depth research on how soil liquefaction can impact pipeline stability (Sumer et al. 1999; Damgaard and Palmer 2001). Relevant outcomes of these research efforts are nowadays reflected by existing industry design guidelines (DNV 2007a, b). As pipeline routes can hardly avoid all liquefiable areas, geotechnical input to pipeline design must include (1) an assessment of liquefaction susceptibility (De Groot et al. 2006); and (2) the prediction of pipe displacement possibly induced by soil liquefaction (Bonjean et al. 2008; Erbrich and Zhou 2017; Bizzotto et al. 2017).

This paper concerns the analysis of buried pipelines interacting with liquefied sand. A novel computational fluid dynamics (CFD)-based approach is proposed to predict postliquefaction pipe displacement, accounting for large deformations and reconsolidation effects in the soil. To prioritize applicability, the large-deformation modeling of liquefied sand as a two-phase mixture was not pursued. Such an endeavor was discouraged by the many questions still open about applying traditional soil mechanics to fluidized geomaterials. Instead, a one-phase approach was preferred, combining Bingham CFD modeling and a separate analysis of pore pressure dissipation. As detailed in the following, the latter aspect enables one to incorporate a phenomenological enhancement of rheological soil properties in the early postliquefaction phase. While the emphasis is on the formulation and validation of the proposed framework, its applicability to both submarine and onshore infrastructures is noted—a relevant example of the latter case concerns, e.g., the seismic analysis of buried lifelines (Akiyoshi and Fuchida 1984; Ling et al. 2003; Yasuda and Kiku 2006; Chian and Madabhushi 2012; Kruse et al. 2013).

¹Assistant Professor, Faculty of Civil Engineering and Geosciences, Delft Univ. of Technology, Stevinweg 1, 2628 CN Delft, Netherlands (corresponding author). ORCID: <https://orcid.org/0000-0001-7648-0280>. Email: f.pisano@tudelft.nl

²Associate Professor, Dept. of Civil and Environmental Engineering, Politecnico di Milano, piazza L. da Vinci 32, 20133 Milano, Italy.

³Associate Professor, Dipartimento di Scienze della Terra 'A. Desio,' Università degli Studi di Milano, via L. Mangiagalli 34, 20133 Milano, Italy. ORCID: <https://orcid.org/0000-0002-9528-0249>

⁴Associate Professor, Dept. of Civil and Environmental Engineering, Politecnico di Milano, piazza L. da Vinci 32, 20133 Milano, Italy.

Note. This manuscript was submitted on February 5, 2020; approved on May 26, 2020; published online on August 11, 2020. Discussion period open until January 11, 2021; separate discussions must be submitted for individual papers. This paper is part of the *Journal of Engineering Mechanics*, © ASCE, ISSN 0733-9399.

CFD Modeling of Liquefied Sand Interacting with Buried Pipes

This section presents the conceptual background and formulation of the proposed modeling approach, including a critical discussion of relevant assumptions.

Conceptual Background

Soil–structure interaction problems are usually tackled in the framework of continuum solid mechanics. Despite the particulate nature of soils, continuum theories have successfully supported a general understanding of soil mechanics and its implications in geotechnical/structural design. Even the presence of pore fluid has been well accommodated in the same framework, owing to the notion of effective stress and the associated effective stress principle (Terzaghi 1943). When regarded as (continuum) solids, water-saturated soils exhibit frictional nonlinear behavior and respond to external loads through deformations (both deviatoric and volumetric) that are strongly coupled with pore water flow. Typical design requirements in civil engineering have determined the wide success of small-deformation approaches along with soil plasticity modeling (Muir Wood 2014).

However, the applicability of solid mechanics should be questioned when external loading and hindered water-drainage induce pore pressures that are large enough for the mean effective stress (p') to vanish. The occurrence of the latter event, most easily in shallow soil layers, has drastic implications: typical attributes of solid behavior (grain contacts, shear strength, and stiffness) disappear while the soil begins to flow as a fluidized grain–water mixture. Such flow is nearly incompressible, rate-dependent, and inevitably associated with large deformations (Guoxing et al. 2016). It should be noted that the transition from the solid-like to fluid-like state is not irreversible, as water drainage and pore pressure dissipation (so-called reconsolidation) can eventually reestablish grain contacts and frictional solid-like behavior.

Recent research efforts have been spent to unify the constitutive modeling of granular materials in their solid, transitional, and fluid states (Andrade et al. 2012; Prime et al. 2014; Vescovi et al. 2020). However, the application of such approaches to boundary value problems is still far from trivial, also due to the dearth of numerical methods and software able to cope with two-phase media and deformations of any magnitude.

A practice-oriented approach is proposed to analyze the interaction between buried pipes and liquefied sand. The following simplifying assumptions were formulated in light of relevant experimental evidence:

- For practical purposes, it is possible to idealize liquefied sand as a one-phase, non-Newtonian viscous fluid and analyze its flow using CFD (see the “CFD Formulation and Numerical Solution” section and equations therein);
- At the onset of postliquefaction reconsolidation, even the moderate dissipation of pore pressure can significantly affect the behavior of liquefied sand. Although genuinely hydro-mechanical, such mechanisms can be phenomenologically captured within the same one-phase fluid framework through suitable variations of rheological properties [Eqs. (4) and (5)]; and
- Postliquefaction pore pressures needed for the update of liquefied sand’s Bingham rheological properties can be separately estimated through a two-phase, small-deformation analysis of reconsolidation [Eqs. (11) and (12)].

Rheology of Liquefied Sand

The study of fluidized soils, including liquefied sand, has attracted numerous researchers with an interest in earthquake engineering (Seed et al. 1976; Stark and Mesri 1992; Tamate and Towhata 1999; Olson and Stark 2002) and/or the propagation of flow slides and debris flows (Pierson and Costa 1987; Uzuoka et al. 1998; Parsons et al. 2001). Although their nature is intrinsically multi-phase, one-phase CFD modeling has gained wide popularity, e.g., for the simplified simulation of debris avalanches (Boukpeti et al. 2012; Pastor et al. 2014) or seismic lateral spreading (Uzuoka et al. 1998; Hadush et al. 2000; Montassar and de Buhan 2013). In fact, adopting a one-phase approach brings about significant modeling advantages while preserving, if properly implemented, features of behavior relevant to engineering applications. The advantages of this approach include (1) a simpler formulation of (one-phase) field equations and constitutive relationships (without two-way hydromechanical coupling), (2) reduced computational costs, and (3) no numerical difficulties related to vanishing effective stresses when soil liquefaction occurs.

Soil–water mixtures with a high solid concentration (i.e., beyond 35% in volume) are most often modeled as non-Newtonian Bingham fluids (O’Brien and Julien 1988). Accordingly, the relationship between deviatoric stress and strain rate tensors is assumed to be linear above a so-called yield stress, below which no flow occurs. In the case of one-dimensional shear flow, the Bingham model reads as a simple uniaxial relationship between the shear stress (τ) and shear strain rate ($\dot{\gamma}$)

$$\begin{aligned} \tau &= \tau_y + \eta \dot{\gamma} & \text{if } \tau > \tau_y \\ \dot{\gamma} &= 0 & \text{otherwise} \end{aligned} \quad (1)$$

where η and τ_y represent the viscosity and yield stress of the fluidized soil, respectively. In the case of two-dimensional/three-dimensional (2D/3D) flow problems, a multiaxial representation of stresses and strain rates is necessary

$$\begin{aligned} \sigma_{ij} &= s_{ij} + p \delta_{ij} \\ \dot{\epsilon}_{ij} &= \dot{e}_{ij} + \frac{\dot{\epsilon}_{\text{vol}}}{3} \delta_{ij} \end{aligned} \quad (2)$$

where the stress (σ_{ij}) and strain rate ($\dot{\epsilon}_{ij}$) tensors decomposed into their deviatoric (s_{ij} and e_{ij}) and isotropic (p and $\dot{\epsilon}_{\text{vol}}$) components; and δ_{ij} = second-order identity tensor. Accordingly, Eq. (1) can be generalized as follows (Cremonesi et al. 2011):

$$\begin{aligned} s_{ij} &= \tau_y \frac{\dot{e}_{ij}}{\|\dot{e}_{ij}\|} + 2\eta \dot{e}_{ij} & \text{if } \|s_{ij}\| > \tau_y \\ \dot{e}_{ij} &= 0 & \text{otherwise} \end{aligned} \quad (3)$$

where $\|s_{ij}\| = \sqrt{(1/2)s_{ij}s_{ij}}$ and $\|\dot{e}_{ij}\| = \sqrt{(1/2)\dot{e}_{ij}\dot{e}_{ij}}$ are the norms of the deviatoric stress and strain rate tensors, respectively. The total ($\dot{\epsilon}_{ij}$) and deviatoric (\dot{e}_{ij}) strain rate tensors coincide in the case of incompressible flow, i.e., when $\epsilon_{\text{vol}} = 0$ at all times.

Decades of research have revealed the broad variability of rheological parameters (Tamate and Towhata 1999; Parsons et al. 2001; Hwang et al. 2006), particularly of viscosity. According to Montassar and de Buhan (2013), “obtained data for the equivalent Newtonian viscosity coefficients range between 10^{-1} and 10^7 Pa · s.” Not only intrinsic factors (e.g., soil mineralogy, porosity, and grain size distribution) contribute to such variability but also the lack of standard procedures for the interpretation of laboratory tests (Della Vecchia et al. 2019).

Enhancement of Rheological Properties during Reconsolidation

The large permeability of sandy soils often enables water drainage soon after liquefaction. As a consequence, pore pressure dissipation and a concurrent increase in mean effective pressure (p') gradually bring the soil back to its solid-like state (reconsolidation). The earliest stage of such a transition is characterized by liquefied sand that still flows as a fluid, although with rheological behavior directly affected by ongoing reconsolidation. Capturing this rapid process is relevant to the analysis of soil–structure interaction, for instance during pipe flotation. To preserve the applicability of Bingham CFD modeling, quantitative information about postliquefaction rheology (i.e., values and time evolution of rheological parameters) should be included in numerical calculations.

Data from experimental studies can be used in support of the above idea, i.e., to describe the dependence of η and τ_y on p' when $r_u < 1$ (Nishimura et al. 2002; Gallage et al. 2005; Guoxing et al. 2016; Chen et al. 2013, 2014; Lirer and Mele 2019) and r_u is the ratio between the current pore pressure and the preliquefaction effective mean stress p'_0 . Particularly meaningful is the work of Gallage et al. (2005), who inferred Bingham properties by subjecting sand specimens at low p' to steps of axial compression at a constant pore pressure. Fig. 1 displays values of η and τ_y measured for low mean effective stress, with p' lower than 20 kPa—note that such low values are fully representative of soil effective stresses near the onset of liquefaction. Small increments in p' produce a remarkable increase in η and τ_y , especially when compared to values extrapolated for $p' = 0$ ($r_u = 1$). All the tests performed by Gallage et al. (2005) show pronounced viscous behavior at a very low p' , which corroborates the assumption of fluid-like sand behavior also in the early postliquefaction phase.

As for CFD modeling, the data in Fig. 1 suggest that both τ_y and η may be split into two components

$$\tau_y = \tau_y^0(r_u = 1) + \tau_y^{\text{rec}}(r_u, p'_0) \quad (4)$$

$$\eta = \eta^0(r_u = 1) + \eta^{\text{rec}}(r_u, p'_0) \quad (5)$$

where τ_y^0 and η^0 material parameters are related to fully liquefied conditions ($r_u = 1$); and τ_y^{rec} and η^{rec} variable components evolve

during reconsolidation, i.e., as p' gradually increases from zero. τ_y^{rec} may be physically associated with the recovery of shear strength

$$\tau_y^{\text{rec}} = A_{\tau_y} p' \approx \frac{M}{\sqrt{3}} p' \quad (6)$$

Fig. 1(a) supports the idea of linking the material coefficient A_{τ_y} to the critical stress ratio M of the fully reconsolidated soil, which lies in the 0.9–1.4 range for friction angles between 25° and 35°. The factor $1/\sqrt{3}$ in Eq. (6) is consistent with the multiaxial formulation in Eq. (3) of a circular yield criterion in the deviatoric π -plane. It should also be noted that as r_u decreases, τ_y^{rec} quickly grows much larger than τ_y^0 , the latter being reported to be usually lower than 100 Pa in fully liquefied sand (O'Brien and Julien 1988; Uzuoka et al. 1998; Parsons et al. 2001; Pierson 2005).

The (rare) data in Fig. 1(b) hint to adopt, as a first approximation, the linear p' -dependence for η^{rec} as well

$$\eta^{\text{rec}} = A_{\eta} p' \quad (7)$$

where the material parameter A_{η} is unfortunately difficult to identify on a micromechanical basis. Fig. 1(b) indicates A_{η} values in the range of 5–15 Pa · s/Pa.

CFD Formulation and Numerical Solution

The interaction between buried pipe and liquefied sand has been studied throughout this work as a fluid–structure interaction problem. CFD simulations were performed using the particle finite-element method (PFEM) in the version developed by Cremonesi et al. (2010, 2011) after Idelsohn et al. (2004). The PFEM has been widely applied to engineering applications, such as fluid dynamics (Idelsohn et al. 2004; Oñate et al. 2014a), fluid–structure interaction (Idelsohn et al. 2006; Franci et al. 2016; Zhu and Scott 2014), bed erosion (Oñate et al. 2008), manufacturing processes (Oñate et al. 2014b), landslides (Cremonesi et al. 2017) and granular flows (Zhang et al. 2014), and, recently, the simulation of cone penetration in water-saturated soils (Monforte et al. 2017). The PFEM adopts a fully Lagrangian description of free-surface fluid flow, especially suitable for fluid–structure interaction problems.

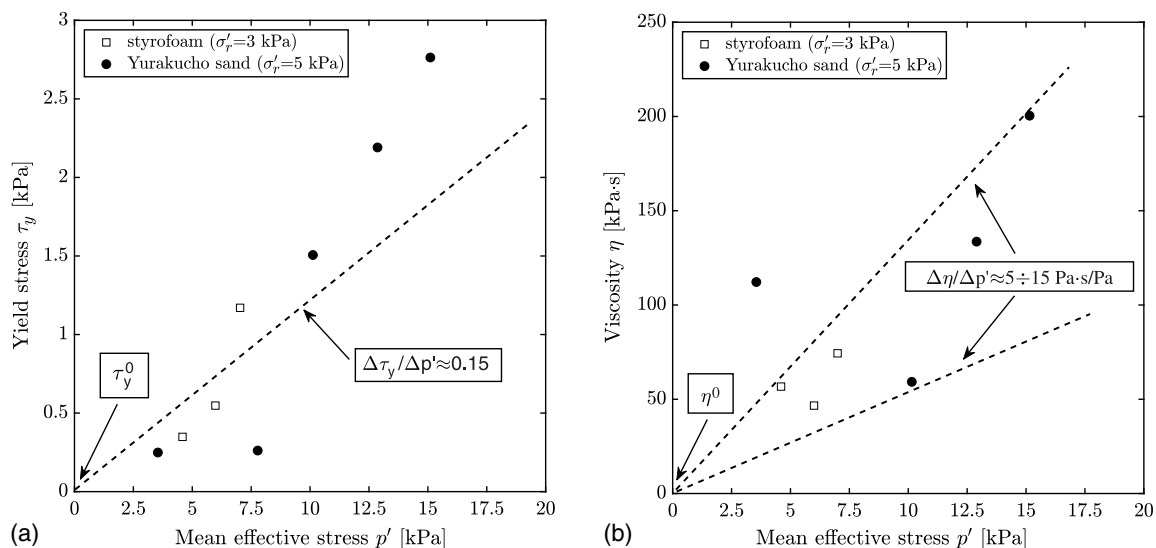


Fig. 1. Dependence of Bingham parameters on mean effective stress, after Gallage et al. (2005)—preliquefaction relative density $D_r \approx 30\%$, and σ'_r stands for radial effective stress.

In a fully Lagrangian framework, the conservation of linear momentum and mass must be fulfilled over the moving fluid volume Ω_t during the time interval $(0, T)$

$$\begin{aligned} \rho \frac{Dv_i}{Dt} &= \sigma_{ij,j} + \rho b_i \quad \text{in } \Omega_t \times (0, T) \\ v_{i,i} &= 0 \quad \text{in } \Omega_t \times (0, T) \end{aligned} \quad (8)$$

where Dv_i/Dt represents the material time differentiation applied to the components of local velocity v_i , while σ_{ij} , ρ , and b_i stand for the total (Cauchy) stress tensor, mass density, and external body force vector, respectively.

Following the PFEM, governing equations were discretized in space with linear interpolation functions for velocity and stress variables; backward Euler time integration was performed along with Newton-type step iterations. The inevitable mesh distortion associated with large deformations was remedied through a remeshing procedure based on the Delaunay tessellation (Cremonesi et al. 2010). A plane-strain 2D version of the previous method was adopted.

The pipe was modeled as a rigid body whose translation in time is governed by the following equilibrium equation:

$$\rho_p A_p \ddot{w}_i = \underbrace{W_i^p}_{\rho_p g_i A_p} + \underbrace{F_i^{\text{fluid}}}_{\int_{\Gamma_p} \sigma_{ij} n_j d\Gamma_p} + \underbrace{F_i^{\text{struct}}}_{-K_{\text{struct}} w_i} \quad (9)$$

where w_i = displacement vector of the pipe centroid; ρ_p and A_p = mass density and cross-section area of the pipe, respectively; and $[g_i] = [0 \ 0 \ -9.81] \text{ m/s}^2$ = gravity acceleration vector. The force terms on the right-hand side relate to the pipe weight (W_i^p), interaction with the fluidized soil (F_i^{fluid}), and other structural restoring forces (F_i^{struct}), respectively. F_i^{fluid} represents the integral of fluid stresses (σ_{ij}) along the lateral surface of the pipe (Γ_p , with n_j its normal unit vector) and includes both buoyancy and drag effects. Whenever applicable, F_i^{struct} reflects the considered structural system and was assumed to linearly depend on w through a (case-specific) elastic stiffness K_{struct} . The rotational degree of freedom is not relevant to the applications addressed in this work and, therefore, not considered in Eq. (9).

The interaction between the pipe and liquefied sand was captured via a staggered Dirichlet-Neumann scheme (Cremonesi et al. 2010). At each time step, the velocity of the rigid body was applied to the fluid interface as a Dirichlet boundary condition; after solving the CFD problem in the surrounding fluid [Eq. (8)], stresses along the pipe boundary were integrated to obtain the F_i^{fluid} term in Eq. (9) and then the updated location and velocity of the pipe in the PFEM model. This staggered procedure was performed iteratively for each time step until convergence (Fig. 2). Overall, the proposed approach relies on the time-domain solution of Navier-Stokes Eq. (8) for an incompressible Bingham fluid whose yield stress and viscosity are updated in space/time through Eqs. (4)–(7). Such an update is based on the current p' values obtained by separately solving the reconsolidation model described in the following. A synopsis of the proposed approach is provided in Fig. 2.

Pore Pressure Dissipation during Reconsolidation

The numerical solution of the system of Eq. (8) requires a suitable constitutive relationship between stresses and strain rates in the liquefied sand. To this end, Bingham modeling with evolving rheological parameters was adopted to capture reconsolidation effects in the early postliquefaction phase. According to Eqs. (6) and (7), the enhancement of τ_y and η depends on the current effective mean stress p' , which is, in fact, not a variable in the one-phase CFD

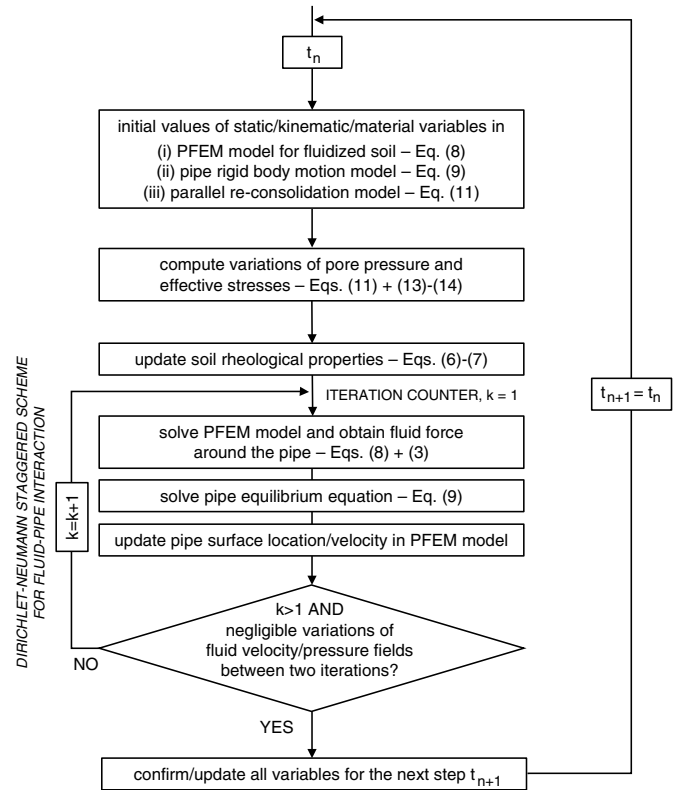


Fig. 2. Solution of a single step in the proposed pipe-soil interaction algorithm.

model. The analyses of the soil–pipe interaction and pore pressure dissipation were therefore decoupled, with the latter reduced in practice to a one-dimensional (1D) problem. This choice corresponds to assuming that the presence of the pipe does not severely affect the pore pressure field (as well as p') in the reconsolidating soil.

Pore pressure dissipation (reconsolidation) in a horizontal soil layer was simulated using Terzaghi's effective stress 1D theory (Terzaghi 1943). Accordingly, the recovery of p' occurs at the expense of the excess pore pressure u_e

$$p'(z, t) = [1 - r_u(z, t)]p'_0 = -\Delta u_e(z, t) \quad (10)$$

for any time (t) and depth below the soil surface (z), starting from the initial condition $p'(z, 0) = 0$ (fully liquefied soil layer). While the bulk of Terzaghi's theory was held valid, some changes were motivated by the highly nonlinear behavior of sand at a very low p' . Indeed, a number of experimental studies show that, during reconsolidation, both the hydraulic conductivity k and 1D oedometer stiffness $E_{\text{oad}} (= 1/m_p, \text{ oedometer compressibility})$ depend strongly on the current effective stress level and void ratio (Brennan and Madabhushi 2011; Haigh et al. 2012; Adamidis and Madabhushi 2016).

The evolution of the excess pore pressure field $u_e(z, t)$ was simulated by solving the following diffusion equation (Adamidis and Madabhushi 2016):

$$\frac{\partial u_e}{\partial t} = \frac{E_{\text{oad}}}{\gamma_w} \frac{\partial}{\partial z} \left(k \frac{\partial u_e}{\partial z} \right) \quad (11)$$

where γ_w represents the unit weight of pore water. Along with u_e , the evolution of the void ratio e [ratio of the volume of the voids to

the volume of solids and related to porosity as $\phi = e/(1 + e)$ was also obtained

$$\frac{\partial e}{\partial t} = \frac{1 + e}{E_{\text{oed}}} \frac{\partial u_e}{\partial t} \quad (12)$$

The empirical relationship proposed by Adamidis and Madabhushi (2016) was adopted for the hydraulic conductivity:

$$k = C_T \frac{e^3}{(1 + e)} [1 + 0.2 \exp(-100\sigma'_v)] \quad (13)$$

where C_T = constitutive parameter; σ'_v = vertical effective stress (in kPa); and k is expressed in m/s. In agreement with empirical evidence (Haigh et al. 2012), the explicit dependence of k on σ'_v appears in Eq. (13).

A number of compression models are available in the literature for the 1D oedometer stiffness, typically implying a power-law dependence on the vertical effective stress σ'_v . Among all, the well-established relationship proposed by Janbu (1963) and reappraised by Muir Wood (2009) was adopted

$$\frac{E_{\text{oed}}}{\sigma'_{\text{ref}}} = \chi \left(\frac{\sigma'_v}{\sigma'_{\text{ref}}} \right)^\alpha \quad (14)$$

where σ'_{ref} = reference effective stress value; and α and χ = two dimensionless material parameters, $0 \leq \alpha \leq 1.5$ and $10^0 \leq \chi \leq 10^6$ (Muir Wood 2009).

Eq. (11) was solved in combination with common initial/boundary conditions:

- Fully liquefied soil layer: $u_e(z, 0) = (\gamma_{\text{sat}} - \gamma_w)z \Rightarrow \sigma'_v(z, 0) = 0$;
- Perfectly draining top boundary: $u_e(0, t) = 0$; and
- Impervious bottom boundary: $\partial u_e / \partial z(H, t) = 0$.

The terms γ_{sat} and H are the saturated unit weight of the soil and the depth of the lower boundary, respectively.

Simulation of Pipe Flotation in Liquefied Sand

Especially relevant to the model validation are the recent tests performed at Deltares (Delft, The Netherlands) to study postliquefaction pipe flotation (Horsten 2016). Pipe flotation experiments were executed in a large container (the length was 4 m, width was 2.5 m, and depth was 1.2 m), equipped with a fluidization system at the bottom to create sand samples of low relative density in the range $D_r = 20\% - 40\%$. Ittebeck sand was used for this purpose, which is a uniform fine sand characterized by $G_s = 2.64$ (specific grain gravity), $D_{50} = 0.165$ mm (median grain diameter), $e_{\text{max}} = 0.868$ (maximum void ratio), and $e_{\text{min}} = 0.527$ (minimum void ratio). Three different high-density polyethylene (HDPE) flexible pipes, with different outer diameter and thickness, were employed. The experimental setup sketched in Fig. 3 featured a fixed-end pipe buried in a saturated sand layer—the clamped edge was introduced to more realistically represent a pipeline connected to an existing structure. Geometrical and mechanical properties of the three pipes are listed in Table 1. More details about the experimental setup can be found in the study by Horsten (2016).

Calibration of Reconsolidation Model

In the original experimental work (Horsten 2016), sand reconsolidation tests were performed prior to flotation experiments. Such tests were performed in a 0.6-m-diameter cylindrical container filled with a 1.2-m-thick layer of saturated loose sand, and the liquefaction was induced by means of single peak vibrations brought about by a falling weight. Pore pressures were measured

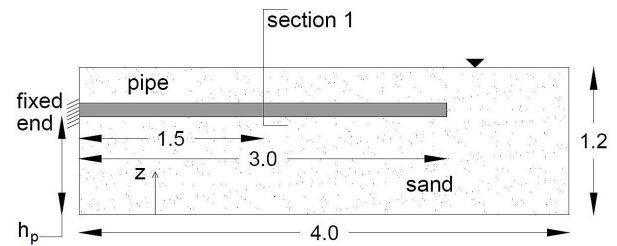


Fig. 3. Sketch of Deltares' experimental setup based on information from Horsten (2016). Dimensions in meters.

Table 1. Pipe geometrical/mechanical properties

Pipe	h_p (mm)	L_p (m)	t_p (mm)	D_p (mm)	A_p (m ²)	I_p (m ⁴)
Pipe 1	790	3	17	110	0.005	$3.5 \cdot 10^{-6}$
Pipe 2	640	3	33	160	0.013	$1.6 \cdot 10^{-5}$
Pipe 3	500	3	33	200	0.017	$2.3 \cdot 10^{-5}$
$\rho_p = 950 \text{ kg/m}^3$ $E_p = 1100 \text{ MPa}$						

Note: h_p = elevation; L_p = length; t_p = cross-section thickness; D_p = outer diameter; A_p = cross-section area; I_p = cross-section moment of inertia; ρ_p = HDPE mass density; and E_p = HDPE Young's modulus.

Table 2. Sets of reconsolidation model parameters used to reproduce experimental measurements from the literature

Set	H (m)	γ (kN/m ³)	C_T (m/s)	e_0	χ	α	σ'_{ref} (kPa)
Set 1	1.2	18.4	$4 \cdot 10^{-4}$	0.88	$7.3 \cdot 10^2$	1.15	100
Set 2	12	18.7	$1.94 \cdot 10^{-3}$	0.84	$2.8 \cdot 10^2$	0.45	100
Set 3	0.4	17.7	$4 \cdot 10^{-4}$	1.04	$0.2 \cdot 10^2$	0.5	100

Note: Calibrated against data from Horsten (2016) (Set 1), Adamidis and Madabhushi (2016) (Set 2), and Towhata et al. (1999) (Set 3).

by five custom-made transducers placed along the depth with 0.2-m regular spacing. Specific reference is made in this study to Sample #2, reportedly characterized by zero initial relative density (the initial void ratio is $e_0 \sim e_{\text{max}}$). The considered reconsolidation tests provided data useful for calibrating the pore pressure dissipation model described previously. Required soil properties and model parameters were directly inferred from Horsten (2016) whenever possible (see Table 2, set 1).

Setting the parameter C_T in Eq. (13) is crucial in that it governs the reference hydraulic conductivity $k_0 = k(\sigma'_v = 0)$, which is not directly measurable. A value of $C_T = 4 \cdot 10^{-4}$ m/s was selected (yielding $k_0 = 1.68 \cdot 10^{-4}$ m/s) to reproduce the timescale of the pore pressure diffusion in the experiment. This value of C_T is about 1/5 of that suggested by Adamidis and Madabhushi (2016) for Hostun sand, reflecting the fact that the latter soil is significantly coarser [$D_{50} = 0.47$ mm, see Haigh et al. (2012)] and more permeable than Ittebeck sand [$D_{50} = 0.17$ mm, see Horsten (2016)].

Regarding the choice of σ'_{ref} , χ , and α in Eq. (14), Muir Wood (2009) provides some broad guidance. Suggested ranges for sand are $10^2 \leq \chi \leq 10^3$, while α varies from 0.2–0.3 (overconsolidated) to 0.4–0.8 (normally consolidated). Reference stress $\sigma'_{\text{ref}} = 100$ kPa [recommended by Muir Wood (2009)] and exponent $\alpha = 1.15$ were set for the Ittebeck sand. A midrange value of $\chi = 5.2 \cdot 10^2$ was selected to complete the parameter calibration.

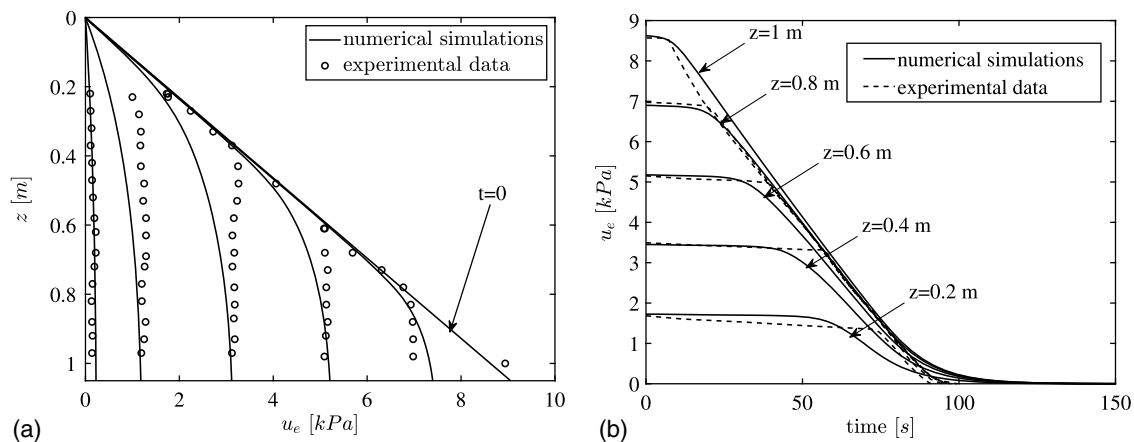


Fig. 4. Simulation of u_e dissipation: (a) u_e isochrones (plotted every 20 s); and (b) u_e time evolution at different depths. (Data from Horsten 2016, Sample #2.)

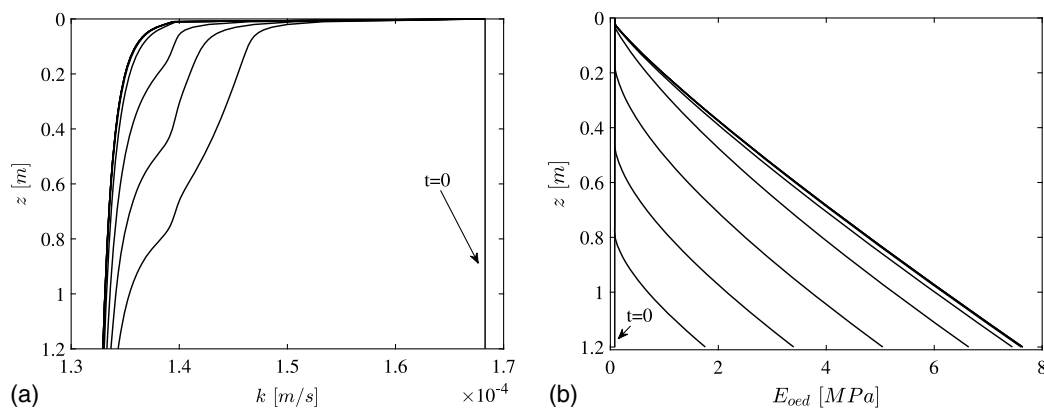


Fig. 5. Isochrones of sand permeability and oedometer stiffness from the simulation of Horsten's (2016) reconsolidation test on Sample #2: (a) permeability isochrones (plotted every 20 s); and (b) oedometer stiffness isochrones (plotted every 20 s).

In Fig. 4(a), the numerical simulations of u_e isochrones are compared to experimental measurements, while Fig. 4(b) shows the simulated and measured time evolution of u_e at four different depths. Both plots exhibit good agreement between computed and measured values. Further insight can be gained from Fig. 5, showing computed isochrones of permeability [Fig. 5(a)] and 1D oedometer stiffness [Fig. 5(b)], respectively. In line with Adamidis and Madabhushi (2016), the overall change in k during reconsolidation is rather small, while E_{oed} experiences large variations. Computed stiffness values appear reasonably close to expected small-stress values for clean sand (Lauder and Brown 2014; Haigh et al. 2012). The performance of the nonlinear pore pressure dissipation model is further discussed in Appendix I with respect to test results provided by Adamidis and Madabhushi (2016).

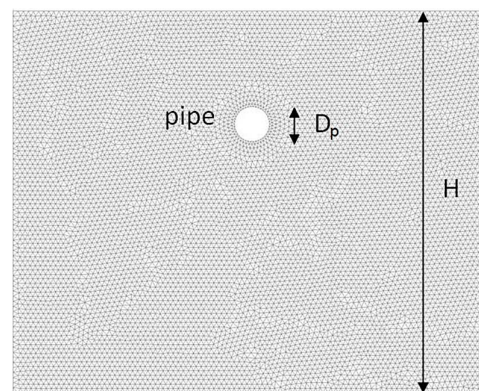


Fig. 6. PFEM mesh for the simulation of Pipe 1's flotation (Table 1).

Pipe Flotation Tests

The three pipes in Table 1 were subjected to separate flotation tests (Horsten 2016). In all cases, the liquefaction of loose Ittebeck sand was achieved through the impact of a weight falling on the sidewall of the rigid container. Resulting displacements of the pipes were measured in time at several locations along their length. As explained in Appendix II, raw flotation measurements first had to be postprocessed to eliminate the effects of spurious rotations caused by imperfect clamping (Horsten 2016).

Flotation tests were numerically simulated using the proposed CFD framework. Two-dimensional plane-strain PFEM models were set up, with the soil domain discretized using linear triangular elements—see mesh in Fig. 6. Velocity no-slip boundary conditions were imposed along all rigid walls along with zero pressure at the top surface. Measured/simulated displacements in Figs. 7–9 relate to the midsection of each pipe (section 1 in Fig. 3). Following Eq. (9), the 3D effect of the clamped edge (Fig. 3) was incorporated in 2D simulations as an elastic restoring force.

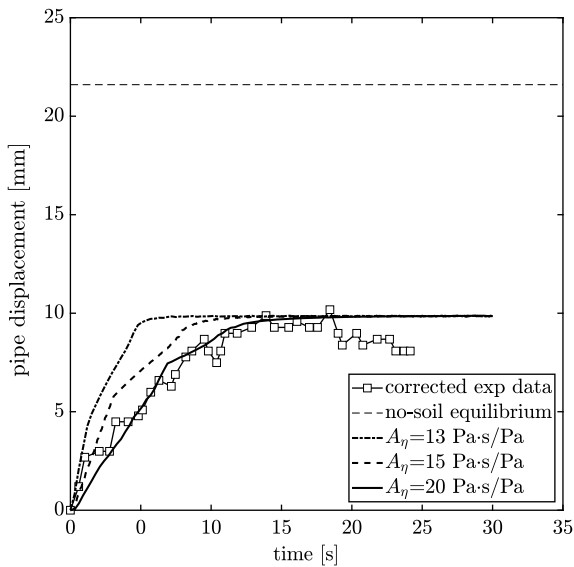


Fig. 7. Pipe 3's flotation: comparison between CFD results and experimental data from Horsten (2016). The theoretical no-soil equilibrium displacement is 21.7 mm.

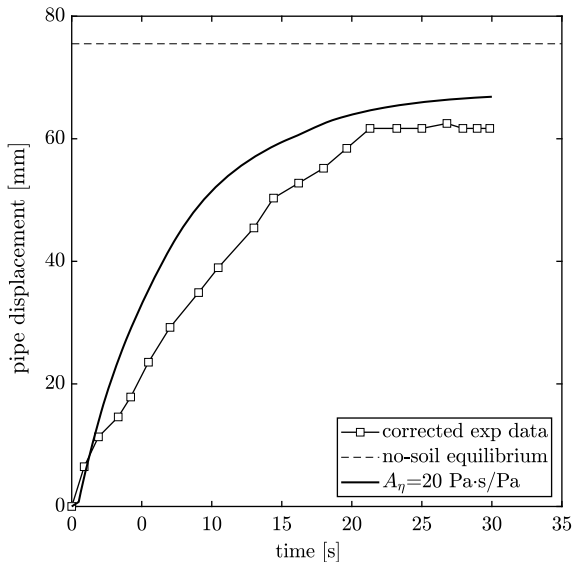


Fig. 8. Pipe 1's flotation: comparison between CFD results and experimental data from Horsten (2016). The theoretical no-soil equilibrium displacement is 75.5 mm.

The structural stiffness $K_{\text{struct}} = (17/384) \cdot L_p^4 / E_p I_p$ associated with the midsection of a cantilever pipe was identified based on standard structural analysis.

Fig. 7 shows how the upward displacement of the 200 mm pipe evolved in time during the test on Pipe 3 (line with square markers). As expected, the general flotation trend features a gradual decrease in pipe velocity until full arrest after about 15 s. The dashed horizontal line in the same figure (the no-soil equilibrium) represents the equilibrium that the same elastic cantilever would theoretically attain under self-weight and fluid buoyancy only. Such an equilibrium allows one to appreciate the influence of shear drag.

While the total mass density ρ was directly obtained from available measured soil data (Table 2, set 1), enhanced Bingham

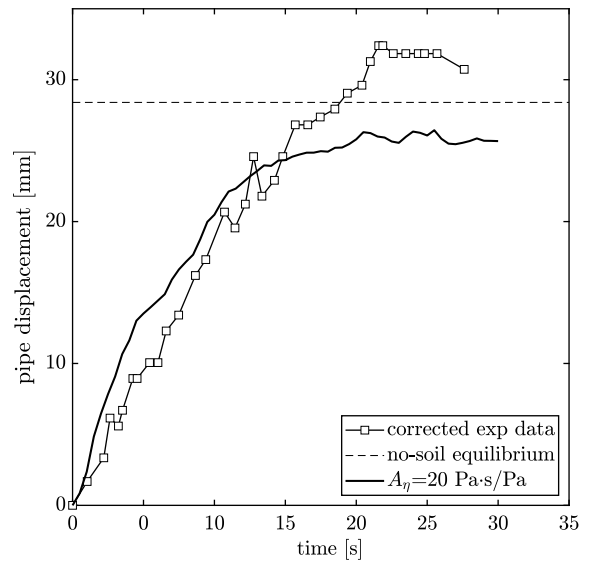


Fig. 9. Pipe 2's flotation: comparison between CFD results and experimental data from Horsten (2016). The theoretical no-soil equilibrium displacement is 28.4 mm.

Table 3. Enhanced Bingham parameters used to reproduce measurements from pipe flotation and pipe dragging tests

Application	τ_y^0 (kPa)	η^0 (Pa · s)	A_{τ_y}	A_η (Pa · s/Pa)
Pipe flotation	0	2,200	0.6928	20
Pipe dragging	0	300	0.6928	13

Note: Calibrated against data from Horsten (2016) and Towhata et al. (1999).

parameters (τ_y^0 , η^0 , A_{τ_y} , and A_η) were calibrated against the experimental flotation curve in Fig. 7:

- To reduce arbitrariness in calibration, default values $\tau_y^0 = 0$ and $A_{\tau_y} (M = 1.2)$ were set. The former reflects the dominance of the reconsolidation over the low shear strength at $r_u = 1$, and the latter relates to an average (critical state) friction angle of 30° ;
- The initial viscosity $\eta^0 = \eta(r_u \approx 1) = 2200 \text{ Pa} \cdot \text{s}$ was selected to capture the pipe velocity at the onset of the flotation; and
- The last parameter A_η was identified to match the general trend and final equilibrium of the flotation during reconsolidation.

A very satisfactory agreement between the experimental and numerical results was achieved for $\eta^0 = 2200 \text{ Pa} \cdot \text{s}$ and $A_\eta = 20 \text{ Pa} \cdot \text{s/Pa}$. The influence of A_η was also parametrically studied to highlight the influence of viscosity enhancement on the timing of pipe flotation (Fig. 7). It is worth noting the good consistency between the set of identified parameters (Table 3) and the previous inferences from Gallage et al.'s (2005) test results (Fig. 1).

Comparing the timing of pipe flotation (Fig. 7) and pore pressure dissipation (Fig. 4) leads to recognition of the substantial influence of early reconsolidation on the final displacement of Pipe 3. Even though pore pressures dissipate only slightly in the first 30 s of the experiment (by about 100 Pa), substantial regains in yield stress and viscosity emerge from Eqs. (6) and (7).

With the same set of calibrated parameters, similar PFEM simulations were performed to predict the uplift experienced by the midsections of Pipes 1 and 2. The corresponding plots in Figs. 8 and 9 confirm a very satisfactory agreement between

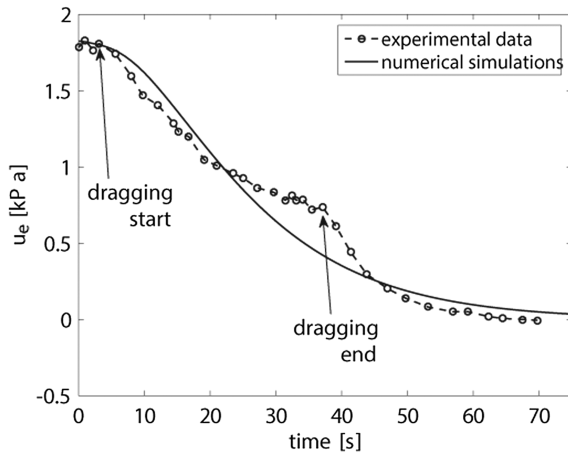


Fig. 10. Simulation of u_e dissipation during pipe lateral dragging. (Data from Towhata et al. 1999.)

experimental and numerical results. The proposed CFD model appears capable of accommodating different degrees of reconsolidation effects for pipes of different sizes, weights, and stiffnesses.

Simulation of Lateral Pipe Dragging in Liquefied Sand

The proposed CFD framework was further validated against the lateral pipe dragging experiments presented by Towhata et al. (1999). Reference is made to a 1-g physical model test in which a pipe embedded in extremely loose saturated sand was laterally dragged at a constant elevation after a full liquefaction induced by a strong shaking of the container [see Section 2 of Towhata et al. (1999) for details]. Towhata et al.'s (1999) experiment was carried out on Toyoura sand, reportedly characterized by $G_s = 2.65$, $D_{50} = 0.17$ mm, and the initial void ratio $e_0 = 1.04$. A 30-mm-diameter and 300-mm-long model pipe was embedded at a 300-mm depth (constant during pipe dragging) in a sand stack of a 400-mm thickness. Pipe dragging was enforced during

postliquefaction pore pressure dissipation, while pure reconsolidation experiments on Toyoura sand (such as those in Fig. 4) were not performed.

Despite high experimental uncertainties and limitations in reported data (Towhata et al. 1999), the 1D reconsolidation model was rather easily calibrated by deducing the initial soil's unit weight from e_0 and G_s and selecting a value of $C_T = 4 \cdot 10^{-4}$ for the Toyoura sand. This is consistent with the value chosen for Ittebeck sand, which has the same particle mean diameter and a likely similar permeability. Soil parameters in Eq. (14) were set within typical ranges after Muir Wood (2009)—see Table 2, set 3. Fig. 10 shows the time evolution of simulated and measured excess pore pressure (at the top of the pipe), starting from the initial full liquefaction. The beginning and end of the pipe dragging are marked on the experimental curve. Pore pressure dissipation is globally well reproduced, although a slight offset between simulated and experimental curves is noticeable when pipe dragging is arrested.

After calibrating the pressure dissipation model, enhanced Bingham parameters were identified for liquefied Toyoura sand. For this purpose, the experimental force–time curve obtained by Towhata et al. (1999) for a lateral dragging velocity of 8 mm/s and the same (preliquefaction) void ratio $e_0 = 1.04$ was used. The same previous values of τ_y^0 and A_{τ_y} were reused to limit freedom in the calibration, while η^0 and A_η were identified as follows:

- The initial viscosity $\eta^0 = \eta(r_u \approx 1) = 300$ Pa · s was selected to capture the drag force values at the beginning of lateral dragging; and
- The last parameter A_η was identified to reproduce the increase in the drag force during reconsolidation.

PFEM simulations were set up with a pipe initially still for the first 4 s, allowing for some reconsolidation to occur before lateral dragging (Fig. 10). In the absence of any structural connections, $F_i^{\text{struct}} = 0$ was set in Eq. (9) for the laterally dragged pipe. Fig. 11(a) shows satisfactory agreement between experimental and numerical curves in terms of drag force per unit length. The relevance of reconsolidation stands out when considering the results of a purely Newtonian simulation ($\tau_y^0 = A_{\tau_y} = A_\eta = 0$ and $\eta^0 = 300$ Pa · s): without regain in shear resistance, the drag force during pipe dragging at constant velocity would barely vary.

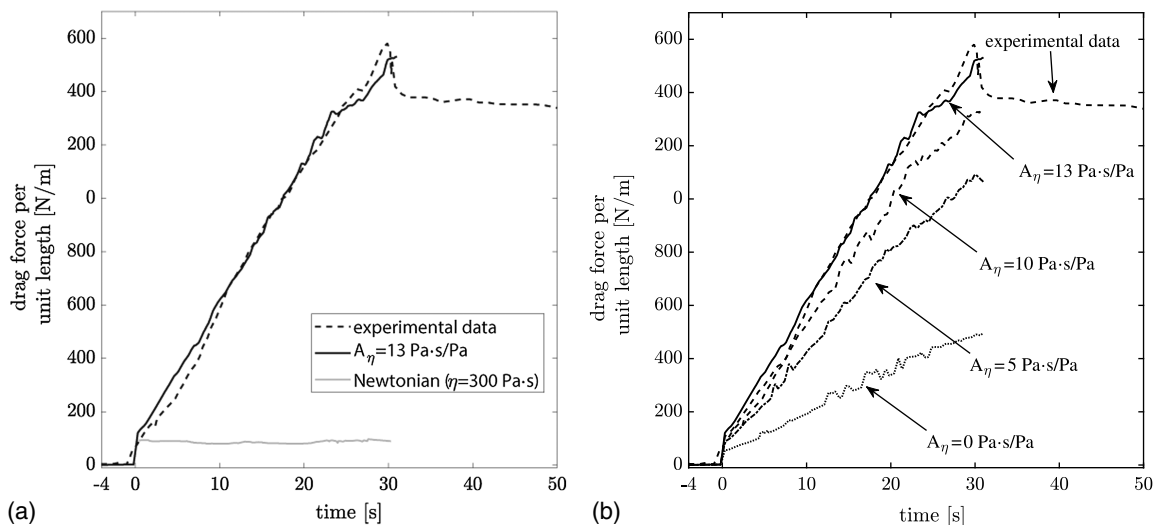


Fig. 11. Lateral pipe dragging: comparison between results from experiments and enhanced Bingham simulations at constant dragging velocity (8 mm/s) and $e_0 = 1.04$: (a) calibration of the enhanced Bingham model; and (b) influence of the A_η parameter. (Data from Towhata et al. 1999.)

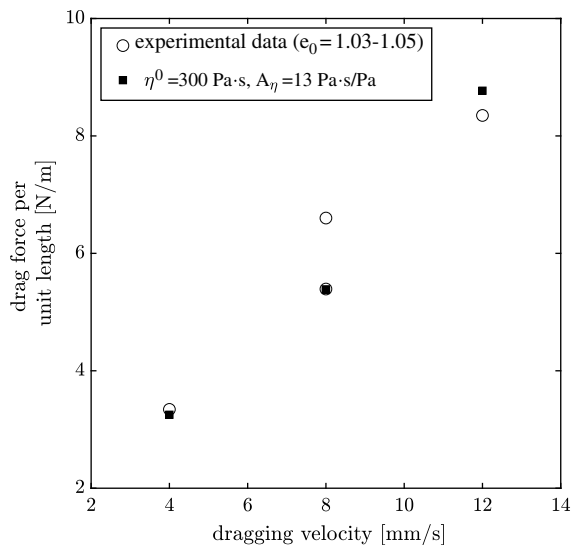


Fig. 12. Lateral pipe dragging: influence of pipe velocity on drag force prior to reconsolidation ($r_u \approx 1$). (Data from Towhata et al. 1999.)

Identified Bingham parameters proved again consistent with existing knowledge on liquefied sand rheology. Particularly, the viscosity enhancement coefficient ($A_\eta = 13 \text{ Pa} \cdot \text{s}/\text{Pa}$) falls exactly within the range indicated by Gallage et al.'s (2005) data in Fig. 1(b), which is also very close to the value calibrated to reproduce Horsten's (2016) flotation tests. The influence of A_η on the increase in the drag force is parametrically demonstrated in Fig. 11(b). The same figure also shows that the effect of increasing viscosity [η^{rec} , Eq. (5)] prevails over the regain of the shear strength, as shown by the relatively low force associated with $A_\eta = 0$ (i.e., with an increase in τ_y only). Although no specific calibration of A_{τ_y} was attempted, the tentative value in Table 3 is of the same order of magnitude suggested by Gallage et al.'s (2005) data [Fig. 1(a)].

The data by Towhata et al. (1999) provided further model validation regarding the relationship between the drag force and dragging velocity. Experimental tests were performed for sand samples with $e_0 = 1.03\text{--}1.05$ and three different velocities, namely, 4, 8, and 12 mm/s. Fig. 12 illustrates the comparison between experimental and numerical results, showing a satisfactory simulation of rate effects.

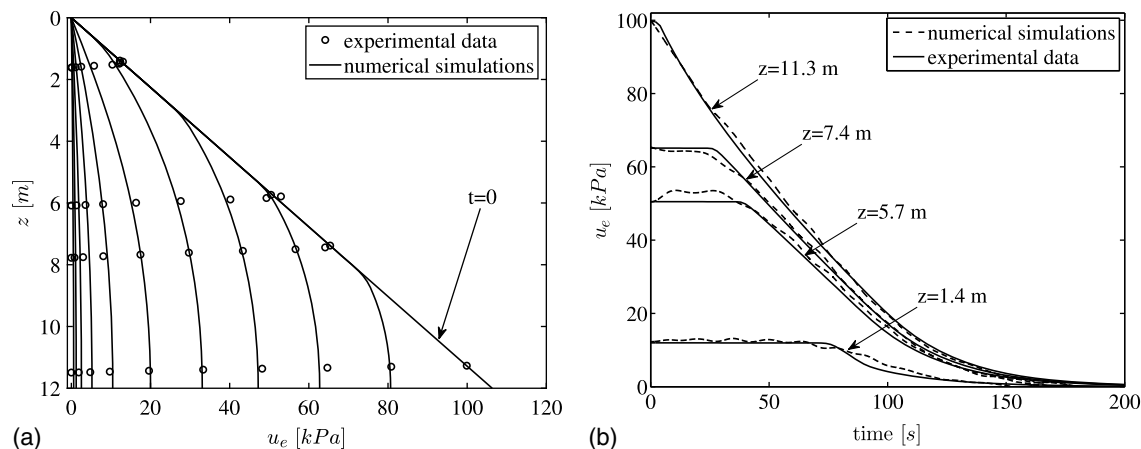


Fig. 13. Simulation of u_e dissipation: (a) u_e isochrones (plotted every 20 s); and (b) u_e time evolution at different depths. (Data from Adamidis and Madabhushi 2016, test OA2-EQ2.)

Concluding Remarks

This work presented a CFD-based approach to analyze the interaction between buried pipelines and liquefied sand, accounting for transient reconsolidation effects. Advanced PFEM simulations were performed in combination with enhanced Bingham modeling of the fluidized soil. The rheological enhancement consisted of an update in space and time of both viscosity and yield strength based on a separate nonlinear analysis of pore pressure dissipation. The result was a Lagrangian CFD framework capable of dealing with large deformations and reconsolidation without explicit modeling of the transition from fluid-like to solid-like behavior.

The soundness of the proposed approach and related calibration procedures were investigated with reference to the experimental literature regarding the interaction of buried pipes with liquefied sand. It was shown that capturing the regain in yield stress and viscosity induced by reconsolidation impacts positively the evaluation of interaction forces and/or displacements experienced by pipes moving through liquefied sand.

The main novelty of this work is the development of a practice-oriented, simplified numerical framework for the analysis of pipeline–soil interaction in the event of soil liquefaction, without the need to model phase transitions in multiphase geomaterials. The main model limitations can be considered to be (1) the one-dimensionality of the pore pressure diffusion model; and (2) the phenomenological nature of the proposed law linking rheological parameters to pore pressure variations. Hence, further improvements may be achieved by (1) using 2D/3D pore pressure diffusion models to deal with more complex geometries and boundary conditions; and (2) reinforcing the micromechanical link between viscosity enhancement and pore pressure dissipation.

The underlying large deformation approach is also expected to suit other flotation triggering mechanisms, e.g., those associated with underwater backfilling of pipeline trenches.

Appendix I. Further Validation of the Pore Pressure Dissipation Model

The above pore pressure dissipation model was further tested against the measurements recorded by Adamidis and Madabhushi (2016) during reconsolidation centrifuge tests on Hostun sand—experiment OA2-EQ2. Selected parameters for this case are given in Table 2—set 2, most of which are taken from published values.

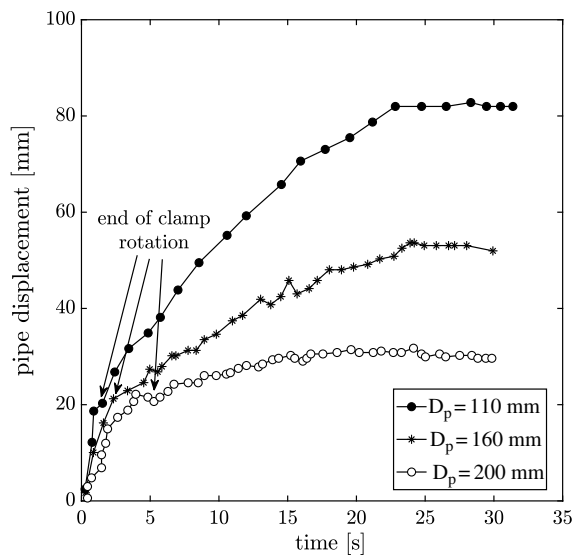


Fig. 14. Raw flotation curves for Pipes 1, 2, and 3. (Data from Horsten 2016.)

Midrange values for sand were assigned to χ and α following Muir Wood (2009). Simulated pore pressure isochrones and time profiles are compared in Fig. 13 to experimental data. Despite the simplicity of the 1D stiffness model in Eq. (14), all key features of reconsolidation are adequately captured.

Although all lying within expected ranges, the two parameter sets in Table 2 exhibit differences due to the sand type and, likely, to the adopted physical modeling strategy (1 g versus centrifuge modeling).

Appendix II. Correction of Raw Flotation Data

The original work of Horsten (2016) reported imperfect clamping of the pipe cantilever (Fig. 3). As a consequence of such imperfection, all pipes experienced a component of rigid rotation during flotation, on average of about 0.9° , i.e., approximately 20 mm of additional displacement at the midsection. This effect is readily visible in the raw displacement data provided by Horsten (2016) and plotted in Fig. 14. In order to simplify PFEM simulations, it was decided to postprocess the raw measured data and eliminate the effect of the undesired rigid rotation. In all cases, it was straightforward to identify and remove the affected branch in each flotation curve, indicated in Fig. 14 as the end of the clamp rotation. Relevant bending was assumed to begin for each pipe at the end of the rigid rotation and corresponded with the corrected experimental data plotted in Figs. 7–9. To approximate actual experimental conditions, PFEM simulations were set up with initial conditions consistent with the after-rotation configuration, i.e., including a higher initial elevation of the pipe, nonzero initial velocity, and sand reconsolidation already developed to some extent.

Data Availability Statement

All data, models, or code that support the findings of this study are available from the corresponding author upon reasonable request. These include the numerical simulation results plotted in the manuscript, numerical code for soil–pipe CFD simulations, and numerical code for the pore pressure dissipation analysis.

Acknowledgments

Input from Omar Zanolli (Rina Consulting) is gratefully acknowledged, as well as the support for numerical simulations provided by former Master of Science students Francesco Bortolotto (AVENTA group) and Kelys Betancur Iglesias (Cathie Associates).

Notation

The following symbols are used in this paper:

- A_p = pipe cross-section area;
- A_{τ_y} = constitutive parameter accounting for yield stress enhancement during reconsolidation;
- A_η = constitutive parameter accounting for viscosity enhancement during reconsolidation;
- b_i = body force vector;
- C_T = hydraulic conductivity parameter;
- D_p = pipe diameter;
- D_r = relative density;
- D_{50} = median soil particle diameter;
- E_{oed} = 1D oedometer stiffness;
- E_p = pipe Young modulus;
- e = void ratio;
- \dot{e}_{ij} = deviatoric strain rate tensor;
- e_{max} = maximum void ratio;
- e_{min} = minimum void ratio;
- F_i^{fluid} = fluid force on pipe (per unit length);
- F_i^{struct} = structural restoring force on pipe (per unit length);
- G_s = relative unit weight of soil grains;
- g_i = gravity acceleration vector;
- H = thickness of the consolidating layer;
- h_p = pipe elevation;
- I_p = moment of inertia of pipe cross-section;
- k = hydraulic conductivity;
- L_p = pipe length;
- M = soil critical stress ratio;
- m_v = 1D oedometer compressibility;
- n_i = unit vector normal to lateral surface of pipe;
- p = mean total stress;
- p' = mean effective stress;
- p'_0 = initial mean effective stress;
- r_u = ratio between current pore pressure and initial mean effective stress;
- s_{ij} = deviatoric stress tensor;
- T = end time of soil–pipe simulations;
- t = time;
- t_p = pipe thickness;
- u_e = excess pore water pressure;
- v_i = velocity vector in soil domain;
- W_p = pipe weight (per unit length);
- w_i = pipe displacement vector;
- z = depth below soil surface;
- α = soil stiffness parameter;
- Γ_p = pipe perimeter;
- $\dot{\gamma}$ = shear strain rate;
- γ_w = water unit weight;
- δ_{ij} = Kronecker identity tensor;
- $\dot{\epsilon}_{ij}$ = strain rate tensor;
- $\dot{\epsilon}_{\text{vol}}$ = volumetric strain rate;

η = viscosity;
 η^{rec} = viscosity enhancement during reconsolidation;
 η^0 = viscosity of fully liquefied soil;
 ρ = soil mass density;
 ρ_p = pipe mass density;
 σ_{ij} = Cauchy stress tensor;
 σ'_r = radial component of effective stress;
 σ'_{ref} = reference effective stress;
 σ'_v = vertical component of effective stress;
 τ = shear stress;
 τ_y = yield shear stress;
 τ_y^{rec} = yield shear stress enhancement during reconsolidation;
 τ_y^0 = yield shear stress of fully liquefied soil;
 ϕ = porosity;
 χ = soil stiffness parameter; and
 Ω_t = moving fluid volume.

References

- Adamidis, O., and G. Madabhushi. 2016. "Post-liquefaction reconsolidation of sand." *Proc. R. Soc. London, Ser. A* 472 (2186): 20150745. <https://doi.org/10.1098/rspa.2015.0745>.
- Akiyoshi, T., and K. Fuchida. 1984. "Soil-pipeline interaction through a frictional interface during earthquakes." *Int. J. Soil Dyn. Earthquake Eng.* 3 (1): 27–34. [https://doi.org/10.1016/0261-7277\(84\)90024-X](https://doi.org/10.1016/0261-7277(84)90024-X).
- Andrade, J. E., Q. Chen, P. H. Le, C. F. Avila, and T. M. Evans. 2012. "On the rheology of dilative granular media: Bridging solid- and fluid-like behavior." *J. Mech. Phys. Solids* 60 (6): 1122–1136. <https://doi.org/10.1016/j.jmps.2012.02.011>.
- Bai, Q., and Y. Bai. 2014. *Subsea pipeline design, analysis, and installation*. Houston, TX: Gulf Professional Publishing.
- Bizzotto, T., M. Brown, A. Brennan, T. Powell, and H. Chandler. 2017. "Modelling of pipeline and cable flotation conditions." In Vol. 865 of *Proc., Offshore Site Investigation Geotechnics 8th Int. Conf. Proc.*, 865–871. London: Society for Underwater Technology.
- Bonjean, D., C. Erbrich, and J. Zhang. 2008. "Pipeline flotation in liquefiable soil." In Vol. 19,668 of *Proc., Annual Offshore Tech. Conf.*, Houston: Offshore Technology Conference.
- Boukpeti, N., D. White, and M. Randolph. 2012. "Analytical modelling of the steady flow of a submarine slide and consequent loading on a pipeline." *Géotechnique* 62 (2): 137. <https://doi.org/10.1680/geot.10.P.001>.
- Brennan, A. J., and S. P. Madabhushi. 2011. "Measurement of coefficient of consolidation during reconsolidation of liquefied sand." *Geotech. Test. J.* 34 (2): 139–146.
- Cathie, D., J. Machin, and R. Overy. 1996. "Engineering appraisal of pipeline flotation during backfilling." In *Proc., Offshore Technology Conf.* Houston, TX: Offshore Technology Conference.
- Chen, Y., H. Liu, and H. Wu. 2013. "Laboratory study on flow characteristics of liquefied and post-liquefied sand." Supplement, *Eur. J. Environ. Civ. Eng.* 17 (S1): 23–32. <https://doi.org/10.1080/19648189.2013.834583>.
- Chen, Y., H. Wu, X. Sha, and H. Liu. 2014. "Laboratory tests on flow characteristics of pre-liquefied sand." In *Proc., Int. Efforts in Lifeline Earthquake Engineering*, 600–607. Reston, VA: ASCE.
- Cheuk, C., D. White, and M. D. Bolton. 2008. "Uplift mechanisms of pipes buried in sand." *J. Geotech. Geoenviron. Eng.* 134 (2): 154–163. [https://doi.org/10.1061/\(ASCE\)1090-0241\(2008\)134:2\(154\)](https://doi.org/10.1061/(ASCE)1090-0241(2008)134:2(154)).
- Chian, S., and S. Madabhushi. 2012. "Effect of buried depth and diameter on uplift of underground structures in liquefied soils." *Soil Dyn. Earthquake Eng.* 41 (Oct): 181–190. <https://doi.org/10.1016/j.soildyn.2012.05.020>.
- Cremonesi, M., F. Ferri, and U. Perego. 2017. "A basal slip model for Lagrangian finite element simulations of 3D landslides." *Int. J. Numer. Anal. Methods Geomech.* 41 (1): 30–53. <https://doi.org/10.1002/nag.2544>.
- Cremonesi, M., A. Frangi, and U. Perego. 2010. "A Lagrangian finite element approach for the analysis of fluid–structure interaction problems." *Int. J. Numer. Methods Eng.* 84 (5): 610–630. <https://doi.org/10.1002/nme.2911>.
- Cremonesi, M., A. Frangi, and U. Perego. 2011. "A Lagrangian finite element approach for the simulation of water-waves induced by landslides." *Comput. Struct.* 89 (11–12): 1086–1093. <https://doi.org/10.1016/j.compstruc.2010.12.005>.
- Damgaard, J., and A. Palmer. 2001. "Pipeline stability on a mobile and liquefied seabed: A discussion of magnitudes and engineering implications." In Vol. 4 of *Proc., OMAE 2001: 20th Int. Conf. on Offshore Mechanics and Arctic Engineering*, 195–204. New York: ASME.
- De Groot, M., M. Bolton, P. Foray, P. Meijers, A. Palmer, R. Sandven, A. Sawicki, and T. Teh. 2006. "Physics of liquefaction phenomena around marine structures." *J. Waterway, Port, Coastal, Ocean Eng.* 132 (4): 227–243. [https://doi.org/10.1061/\(ASCE\)0733-950X\(2006\)132:4\(227\)](https://doi.org/10.1061/(ASCE)0733-950X(2006)132:4(227)).
- Della Vecchia, G., M. Cremonesi, and F. Pisanò. 2019. "On the rheological characterisation of liquefied sands through the dam-breaking test." *Int. J. Numer. Anal. Methods Geomech.* 43 (7): 1410–1425. <https://doi.org/10.1002/nag.2905>.
- DNV (Det Norske Veritas). 2007a. *Global buckling of submarine pipelines—Structural design due to high temperature/high pressure*. RP-F110. Oslo, Norway: DNV.
- DNV (Det Norske Veritas). 2007b. *On-bottom stability design of submarine pipelines*. DNV-RPF109. Oslo, Norway: DNV.
- Erbrich, C., and H. Zhou. 2017. "Optimised backfill design for preventing pipeline flotation." In Vol. 872 of *Proc., Offshore Site Investigation Geotechnics 8th Int. Conf. Proc.*, 872–880. London: Society for Underwater Technology.
- Franci, A., E. Oñate, and J. Carbonell. 2016. "Unified Lagrangian formulation for solid and fluid mechanics and FSI problems." *Comput. Methods Appl. Mech. Eng.* 298 (Jan): 520–547. <https://doi.org/10.1016/j.cma.2015.09.023>.
- Gallage, C. P. K., I. Towhata, and S. Nishimura. 2005. "Laboratory investigation on rate-dependent properties of sand undergoing low confining effective stress." *Soils Found.* 45 (4): 43–60. https://doi.org/10.3208/sandf.45.4_43.
- Guoxing, C., Z. Enquan, W. Zhihua, W. Binghui, and L. Xiaojun. 2016. "Experimental investigation on fluid characteristics of medium dense saturated fine sand in pre-and post-liquefaction." *Bull. Earthquake Eng.* 14 (8): 2185–2212. <https://doi.org/10.1007/s10518-016-9907-6>.
- Hadush, S., A. Yashima, and R. Uzuoka. 2000. "Importance of viscous fluid characteristics in liquefaction induced lateral spreading analysis." *Comput. Geotech.* 27 (3): 199–224. [https://doi.org/10.1016/S0266-352X\(00\)00015-X](https://doi.org/10.1016/S0266-352X(00)00015-X).
- Haigh, S. K., J. Eadington, and S. P. G. Madabhushi. 2012. "Permeability and stiffness of sands at very low effective stresses." *Géotechnique* 62 (1): 69–75. <https://doi.org/10.1680/geot.10.P.035>.
- Horsten, T. 2016. "Pipe uplift in liquefied sands." M.S. thesis, Faculty of Civil Engineering and Geosciences, Delft Univ. of Technology.
- Hwang, J.-I., C.-Y. Kim, C.-K. Chung, and M.-M. Kim. 2006. "Viscous fluid characteristics of liquefied soils and behavior of piles subjected to flow of liquefied soils." *Soil Dyn. Earthquake Eng.* 26 (2): 313–323. <https://doi.org/10.1016/j.soildyn.2005.02.020>.
- Idelsohn, S., E. Oñate, and F. D. Pin. 2004. "The particle finite element method: A powerful tool to solve incompressible flows with free-surfaces and breaking waves." *Int. J. Numer. Methods Eng.* 61 (7): 964–989. <https://doi.org/10.1002/nme.1096>.
- Idelsohn, S., E. Oñate, F. D. Pin, and N. Calvo. 2006. "Fluid-structure interaction using the particle finite element method." *Comput. Methods Appl. Mech. Eng.* 195 (17–18): 2100–2123. <https://doi.org/10.1016/j.cma.2005.02.026>.
- Janbu, N. 1963. "Soil compressibility as determined by oedometer and triaxial tests." In Vol. 1 of *Proc., 3rd European Conf. on Soil Mechanics and Foundation Engineering*, 19–25. London: International Society for Soil Mechanics and Geotechnical Engineering London.
- Kruse, H., P. Meijers, C. Costa Ferrer, G. de Lange, T. Vermaas, H. Havinga, J. Landwehr, and A. Heinsbroek. 2013. *Effects of induced earthquakes on the Gasunie network in Groningen*. [In Dutch.] Rep. No. 1208092-000-GEO-0005. Delft, Netherlands: Deltares.

- Lauder, K. L., and M. J. Brown. 2014. "Scaling effects in the 1 g modelling of offshore pipeline ploughs." In *Proc., 8th Int. Conf. on Physical Modelling in Geotechnics 2014*, 377–383. Boca Raton, FL: CRC Press.
- Ling, H. I., Y. Mohri, T. Kawabata, H. Liu, C. Burke, and L. Sun. 2003. "Centrifugal modeling of seismic behavior of large-diameter pipe in liquefiable soil." *J. Geotech. Geoenviron. Eng.* 129 (12): 1092–1101. [https://doi.org/10.1061/\(ASCE\)1090-0241\(2003\)129:12\(1092\)](https://doi.org/10.1061/(ASCE)1090-0241(2003)129:12(1092)).
- Lirer, S., and L. Mele. 2019. "On the apparent viscosity of granular soils during liquefaction tests." *Bull. Earthquake Eng.* 17 (11): 5809–5824. <https://doi.org/10.1007/s10518-019-00706-0>.
- Luan, M., P. Qu, D.-S. Jeng, Y. Guo, and Q. Yang. 2008. "Dynamic response of a porous seabed–pipeline interaction under wave loading: Soil–pipeline contact effects and inertial effects." *Comput. Geotech.* 35 (2): 173–186. <https://doi.org/10.1016/j.compgeo.2007.05.004>.
- Monforte, L., M. Arroyo, J. M. Carbonell, and A. Gens. 2017. "Numerical simulation of undrained insertion problems in geotechnical engineering with the particle finite element method (PFEM)." *Comput. Geotech.* 82 (Feb): 144–156. <https://doi.org/10.1016/j.compgeo.2016.08.013>.
- Montassar, S., and P. de Buhan. 2013. "Numerical prediction of liquefied ground characteristics from back-analysis of lateral spreading centrifuge experiments." *Comput. Geotech.* 52 (Jul): 7–15. <https://doi.org/10.1016/j.compgeo.2013.01.010>.
- Muir Wood, D. 2009. *Soil mechanics: A one-dimensional introduction*. Cambridge, UK: Cambridge University Press.
- Muir Wood, D. 2014. *Geotechnical modelling*. Boca Raton, FL: CRC Press.
- Nishimura, S., I. Towhata, and T. Honda. 2002. "Laboratory shear tests on viscous nature of liquefied sand." *Soils Found.* 42 (4): 89–98. https://doi.org/10.3208/sandf.42.4_89.
- O'Brien, J. S., and P. Y. Julien. 1988. "Laboratory analysis of mudflow properties." *J. Hydraul. Eng.* 114 (8): 877–887. [https://doi.org/10.1061/\(ASCE\)0733-9429\(1988\)114:8\(877\)](https://doi.org/10.1061/(ASCE)0733-9429(1988)114:8(877)).
- Olson, S. M., and T. D. Stark. 2002. "Liquefied strength ratio from liquefaction flow failure case histories." *Can. Geotech. J.* 39 (3): 629–647. <https://doi.org/10.1139/t02-001>.
- Oñate, E., A. Franci, and J. Carbonell. 2014a. "Lagrangian formulation for finite element analysis of quasi-incompressible fluids with reduced mass losses." *Int. J. Numer. Methods Fluids* 74 (10): 699–731. <https://doi.org/10.1002/flid.3870>.
- Oñate, E., A. Franci, and J. Carbonell. 2014b. "A particle finite element method for analysis of industrial forming processes." *Comput. Mech.* 54 (1): 85–107. <https://doi.org/10.1007/s00466-014-1016-2>.
- Oñate, E., S. Idelsohn, M. Celigueta, and R. Rossi. 2008. "Advances in the particle finite element method for the analysis of fluid-multibody interaction and bed erosion in free surface flows." *Comput. Methods Appl. Mech. Eng.* 197 (19–20): 1777–1800.
- Parsons, J. D., K. X. Whipple, and A. Simoni. 2001. "Experimental study of the grain-flow, fluid-mud transition in debris flows." *J. Geol.* 109 (4): 427–447. <https://doi.org/10.1086/320798>.
- Pastor, M., et al. 2014. "Application of a SPH depth-integrated model to landslide run-out analysis." *Landslides* 11 (5): 793–812. <https://doi.org/10.1007/s10346-014-0484-y>.
- Pierson, T. C. 2005. "Hyperconcentrated flow—Transitional process between water flow and debris flow." In *Debris-flow hazards and related phenomena*, 159–202. Berlin: Springer.
- Pierson, T. C., and J. E. Costa. 1987. "A rheologic classification of subaerial sediment-water flows." In Vol. 7 of *Debris flows/avalanches—Process, recognition, and mitigation: Reviews in engineering geology*, 1–12. Boulder, CO: Geological Society of America.
- Pipeline Flotation Research Council. 1966. "ASCE preliminary research on pipeline flotation: Report of the pipeline flotation research council." *J. Pipeline Div.* 92 (1): 27–74.
- Prime, N., F. Dufour, and F. Darve. 2014. "Solid–fluid transition modelling in geomaterials and application to a mudflow interacting with an obstacle." *Int. J. Numer. Anal. Methods Geomech.* 38 (13): 1341–1361. <https://doi.org/10.1002/nag.2260>.
- Seed, H. B., P. P. Martin, and J. Lysmer. 1976. "Pore-water pressure changes during soil liquefaction." *J. Geotech. Geoenviron. Eng.* 102 (GT4): 323–346.
- Stark, T. D., and G. Mesri. 1992. "Undrained shear strength of liquefied sands for stability analysis." *J. Geotech. Eng.* 118 (11): 1727–1747. [https://doi.org/10.1061/\(ASCE\)0733-9410\(1992\)118:11\(1727\)](https://doi.org/10.1061/(ASCE)0733-9410(1992)118:11(1727)).
- Sumer, B. M., J. Fredsøe, S. Christensen, and M. Lind. 1999. "Sinking/floatation of pipelines and other objects in liquefied soil under waves." *Coastal Eng.* 38 (2): 53–90. [https://doi.org/10.1016/S0378-3839\(99\)00024-1](https://doi.org/10.1016/S0378-3839(99)00024-1).
- Tamate, S., and I. Towhata. 1999. "Numerical simulation of ground flow caused by seismic liquefaction." *Soil Dyn. Earthquake Eng.* 18 (7): 473–485. [https://doi.org/10.1016/S0267-7261\(99\)00022-6](https://doi.org/10.1016/S0267-7261(99)00022-6).
- Teh, T., A. Palmer, M. Bolton, and J. Damgaard. 2006. "Stability of submarine pipelines on liquefied seabeds." *J. Waterway, Port, Coastal, Ocean Eng.* 132 (4): 244–251. [https://doi.org/10.1061/\(ASCE\)0733-950X\(2006\)132:4\(244\)](https://doi.org/10.1061/(ASCE)0733-950X(2006)132:4(244)).
- Terzaghi, K. 1943. *Theoretical soil mechanics*, 11–15. New York: Wiley.
- Towhata, I., W. Vargas-Monge, R. Orense, and M. Yao. 1999. "Shaking table tests on subgrade reaction of pipe embedded in sandy liquefied subsoil." *Soil Dyn. Earthquake Eng.* 18 (5): 347–361. [https://doi.org/10.1016/S0267-7261\(99\)00008-1](https://doi.org/10.1016/S0267-7261(99)00008-1).
- Uzuoka, R., A. Yashima, T. Kawakami, and J.-M. Konrad. 1998. "Fluid dynamics based prediction of liquefaction induced lateral spreading." *Comput. Geotech.* 22 (3–4): 243–282. [https://doi.org/10.1016/S0266-352X\(98\)00006-8](https://doi.org/10.1016/S0266-352X(98)00006-8).
- Vescovi, D., P. Marveggio, and C. G. di Prisco. 2020. "Saturated granular flows: Constitutive modelling under steady simple shear conditions." *Géotechnique* 70 (7): 608–620. <https://doi.org/10.1680/jgeot.19.P.023>.
- White, D., and D. Cathie. 2010. "Geotechnics for subsea pipelines." In *Proc., 2nd Int. Symp. on Frontiers in Offshore Geotechnics*, 87–123. Rotterdam, Netherlands: A.A. Balkema.
- Yasuda, S., and H. Kiku. 2006. "Uplift of sewage manholes and pipes during the 2004 Niigataken-Chuetsu earthquake." *Soils Found.* 46 (6): 885–894. <https://doi.org/10.3208/sandf.46.885>.
- Zhang, X., K. Krabbenhoft, and D. Sheng. 2014. "Particle finite element analysis of the granular column collapse problem." *Granular Matter* 16 (4): 609–619. <https://doi.org/10.1007/s10035-014-0505-5>.
- Zhu, M., and M. H. Scott. 2014. "Modeling fluid-structure interaction by the particle finite element method in OpenSees." *Comput. Struct.* 132 (Feb): 12–21. <https://doi.org/10.1016/j.compstruc.2013.11.002>.